Numerical prediction of cavitation erosion in a water-jet propulsion system

Citation for the original published paper (version of record):
Özgünoglu, M., Persson, M., Saber, A. et al (2025). Numerical prediction of cavitation erosion in a water-jet propulsion system. Ocean Engineering, 340.
http://dx.doi.org/10.1016/j.oceaneng.2025.122316

(article starts on next page)

Ocean Engineering 340 (2025) 122316

Contents lists available at ScienceDirect

Ocean Engineering

journal homepage: www.elsevier.com/locate/oceaneng

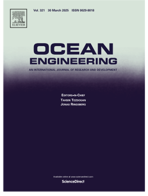

Research paper

Numerical prediction of cavitation erosion in a water-jet propulsion system

Mehmet Özgünoğlu[a,*], Martin Persson[b], Ammar Saber[b], Rickard E. Bensow[a]

[a] Chalmers University of Technology, Gothenburg, Sweden
[b] Kongsberg Maritime Sweden AB, Kristinehamn, Sweden

ARTICLE INFO

Keywords:
CFD
Cavitation erosion
Water-jet pump

ABSTRACT

This study presents a numerical method for predicting erosion in a commercial water-jet pump. The multiphase flow is modeled using the Schnerr-Sauer cavitation model within an unsteady RANS framework, employing the SST k-ω turbulence model. An erosion indicator based on the squared material derivative of pressure, $(DP/Dt)^2$, is used to identify high-risk regions of aggressive cavitation collapse. Three operating conditions are investigated to assess the robustness of the numerical methodology and effect of the operating conditions. This study uniquely examines cavitation erosion risk under multiple operating conditions, providing a comprehensive assessment of numerical prediction methods. The numerical predictions successfully captured erosion-prone regions, showing good agreement with experimental data. However, RANS-based modeling exhibited limitations in resolving transient cavitation structures, leading to an underestimation of erosion extent. Despite the limitations, the proposed RANS-based framework serves as a computationally efficient early-stage assessment tool for cavitation erosion in industrial applications.

1. Introduction

Water-jet propulsion systems are dominant in certain applied marine applications due to their efficiency and superior maneuverability compared to traditional propeller-based propulsion systems (Park et al., 2005). However, cavitation erosion remains a critical concern, leading to material degradation, reduced performance, and higher maintenance costs.

Cavitation occurs when the local pressure drops below the fluid's vapor pressure, causing vapor pockets to form. The subsequent collapse of these cavities generates high-pressure shock waves and micro-jets, potentially damaging nearby surfaces (Franc and Michel, 2004). Despite the extensive research, predicting and mitigating cavitation erosion remains challenging due to the complex interactions between turbulence, multiphase flow behavior, and material responses (Bark and Bensow, 2013).

Experimental methods are essential for understanding and mitigating cavitation erosion. High-speed imaging techniques provide direct visualization of cavitation inception and bubble collapses (Bark et al., 2004). Paint erosion tests help to identify erosion-prone areas (Arabnejad et al., 2022; Aktas et al., 2020), while pressure fluctuation measurements offer insights into cavitation dynamics (Alves Pereira et al., 2024). However, these experimental methods have several limitations. Spatial resolution is often insufficient, making it difficult to correlate observed erosion with specific flow structures. Furthermore, identifying erosion at later stages of the design process often leads to costly modifications, emphasizing the need for accurate early-stage prediction methods (Arabnejad et al., 2022). Computational Fluid Dynamics (CFD) has become an essential tool for overcoming these limitations by providing detailed simulations of cavitation and cavitation erosion mechanisms.

For marine propulsors and hydrofoils, various turbulence models are used for cavitation and cavitation erosion simulations, including Reynolds-Averaged Navier-Stokes (RANS), Detached Eddy Simulation (DES), and Large Eddy Simulation (LES). RANS-based models are commonly used in industrial applications due to their computational efficiency (Melissaris et al., 2019, 2020, 2022; Huang et al., 2021; Li et al., 2014). However, they often struggle to resolve transient cavitation structures and high-frequency pressure fluctuations, both of which are essential for accurate erosion prediction (Bensow, 2021). DES methods combine RANS modeling near walls with LES in separated flow regions, improving accuracy in complex cavitating flows (Usta et al., 2017; Usta and Korkut, 2018; Koksal et al., 2021; Shin and Andersen, 2020). LES models further enhance resolution but require substantial cost, limiting their industrial feasibility (Wheeler et al., 2024). Alternatively, Xu et al. (2024) applied wall-modeled LES (WMLES) to study unsteady flow in water-jet pumps. Their study demonstrated the predictive capability of WMLES while also highlighting its significant computational demands.

In addition to turbulence modeling, multiphase cavitation modeling defines how vapor cavities interact with the surrounding liquid phase.

---

* Corresponding author.
E-mail address: mozgunoglu@gmail.com (M. Özgünoğlu).

https://doi.org/10.1016/j.oceaneng.2025.122316
Received 17 April 2025; Received in revised form 18 July 2025; Accepted 26 July 2025

Eulerian models treat cavitation as a homogeneous mixture, assuming vapor and liquid share the same velocity field. These models are computationally efficient but often fail to resolve individual bubble collapse behavior, which is critical for erosion prediction (Cao et al., 2017; Xu and Lai, 2023). In contrast, Eulerian-Lagrangian models explicitly track individual vapor bubbles, improving predictions of localized collapse pressures, micro-jets, and shock waves (Ji et al., 2024; Wang et al., 2023; Yang et al., 2025).

Most numerical cavitation erosion studies focus on marine propellers and hydrofoils, where erosion is primarily caused by tip vortex cavitation, cloud cavitation, and re-entrant jets. Numerical studies have successfully applied density-based compressible models to resolve collapse-induced impact pressures (Budich et al., 2015). Other approaches have introduced micro-jet impact and energy-based models, validated through soft paint erosion tests and ductile material erosion simulations (Peters et al., 2018; Schenke and van Terwisga, 2019; Shin and Andersen, 2020; Kleinsorge et al., 2022). While these models have significantly improved erosion prediction for propellers, their application to water-jet propulsion systems remains under-explored. However, even with advances in cavitation erosion modeling, existing erosion prediction tools lack the robustness and efficiency needed for routine industrial use (Wheeler et al., 2024). Most previous studies have focused on a single operating condition, limiting their ability to assess cavitation erosion risk comprehensively. This study examines multiple operating conditions, demonstrating that the erosion assessment method remains valid even in cases where significant erosion is not expected.

Unlike propellers, the studies with cavitation modeling for water-jet pumps have primarily focused on performance degradation and flow instabilities rather than direct erosion risk assessment (Cao et al., 2017; Kaixuan et al., 2024; Huang et al., 2021; Xu and Lai, 2023). Previous investigations have examined the effects of non-uniform suction flow and swirl distortion on cavitation inception, showing how secondary flow structures influence cavitation intensity (Cao et al., 2017). Other studies have analyzed blade loading variations and demonstrated that different geometries significantly alter cavitation behavior (Xu and Lai, 2023). Arabnejad et al. (2020) performed LES simulations of the AxWJ-2 axial water-jet pump, identifying tip leakage vortices as a key factor in cavitation development. Water-jet pumps differ from open marine propellers due to their fully wall-bounded, confined, and complex geometries. These conditions significantly increase computational complexity for high-fidelity CFD methods such as LES and DES, especially in near-wall regions where fine mesh resolution is required (Arabnejad et al., 2020, 2022). High-fidelity simulations, although accurate, are often impractical due to their high computational demands (Bensow, 2021). Lower-cost alternatives, such as RANS-based models, require further validation to be applied reliably to cavitating flows. The confined, wall-bounded nature of water-jet propulsion systems makes this validation even more critical (Arabnejad et al., 2022; Wheeler et al., 2024).

Studies specifically assessing cavitation erosion in water-jet pumps remain limited. One of the few examples is Qiu et al. (2021), who proposed the Erosive Power Method (EPM), correlating erosion severity with cavitation collapse intensity. Their approach provided a computationally efficient alternative to high-fidelity simulations but required further validation in complex cavitating flows. Arabnejad et al. (2022) later investigated erosion risks in a different geometry, applying LES and an erosion model based on energy cascading (Arabnejad et al., 2021).

Despite significant advancements in cavitation and erosion modeling, several key challenges persist. The aforementioned studies have demonstrated good agreement between numerical erosion risk predictions and experimental observations. However, the robustness of these models across varying operating conditions remains a concern. Many high-fidelity models provide accurate erosion predictions but are often computationally expensive and complex to integrate into industrial design workflows. This poses a major challenge for industrial applications, where computational efficiency is critical for practical implementation. The trade-off between computational cost and model accuracy continues to be a challenge, as high-fidelity methods such as LES and Eulerian-Lagrangian approaches offer superior resolution but require extensive computational resources. For industrial frameworks, it is essential to develop numerical models that not only provide reliable erosion predictions but also remain computationally feasible for routine engineering design and optimization. Additionally, while cavitation erosion in marine propellers has been extensively studied, the water-jet pumps have received less attention in this regard.

This study aims to develop and validate a computationally efficient cavitation erosion assessment methodology using RANS for water-jet propulsion systems. Building upon previous LES-based studies by Arabnejad et al. (2022), this research investigates the same water-jet pump geometry under different operating conditions with RANS. The proposed overall methodology seeks to balance predictive accuracy and computational feasibility. The cavitation erosion assessment tool is based on the squared material derivative of pressure, $(DP/Dt)^2$, which has been previously validated in fuel injector applications (Özgünoğlu et al., 2025). By comparing RANS and previous LES predictions (Arabnejad et al., 2022) and validating them against experimental paint erosion data, this study aims to provide a practical and reliable tool for early-stage erosion risk assessment in water-jet pump design.

2. Operating conditions and experiments

The experiments were conducted in 2010 at the Kongsberg Hydrodynamic Research Centre (KHRC) in Kristinehamn, Sweden, using their free-surface cavitation tunnel. A soft paint erosion test was used to assess cavitation-induced damage on a mixed-flow pump. The tested impeller was a scaled-down prototype of a commercial water-jet pump, with a model inlet diameter of 200 mm. The impeller was coated with black stencil ink and thinner. Each test lasted one hour under controlled conditions. The removal of paint served as a qualitative indicator of cavitation erosion, identifying regions where cavitation collapse was most aggressive (Alves Pereira et al., 2024).

Table 1 provides an overview of the operating conditions for each case. The tunnel water velocity (v_t) was recorded at a standard position 1400 mm upstream of the inlet lip using tunnel stationary equipment. The tunnel pressure (p_t) was measured in the air volume. The rotation rate was 20 rps for all cases.

The cavitation number (σ) is calculated using the tunnel pressure and tunnel water velocity, as expressed by the following equation:

$$\sigma = \frac{p_t - p_v}{\frac{1}{2}\rho v_t^2} \tag{1}$$

where, p_v is the vapor pressure of water (2065 [Pa]), and ρ is the water density (998.2 [kg/m^3]).

Table 1
Summary of the operating conditions.

Studied case	Tunnel velocity v_t [m/s]	Tunnel pressure p_t [Pa]	Flow rate Q_e [m^3/s]	Cavitation number, σ
Case#1	4.85	18,600	0.14400	1.410
Case#2	7.2	11,800	0.15168	0.376
Case#3	8.7	17,000	0.15648	0.395

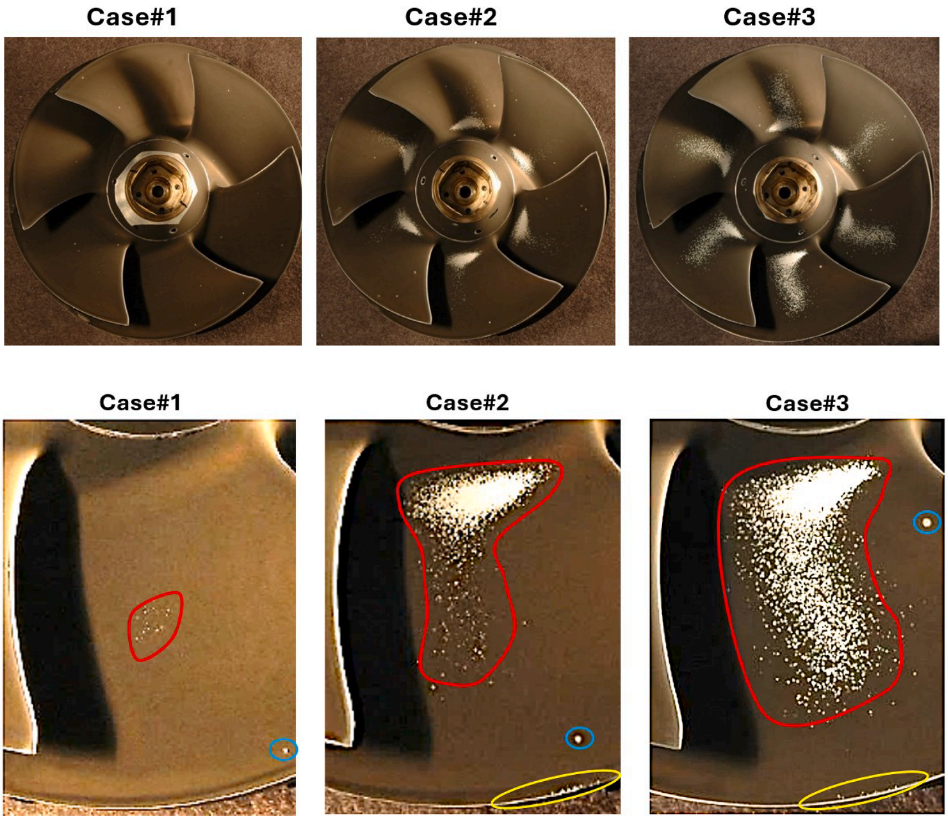

Fig. 1. Erosion patterns for the selected cases. Top row: full impeller view; Bottom row: single blade close-up.

The cases were selected to investigate the distinct erosion patterns unique to each operating condition. This selection provides a robust way to evaluate the predictive capability of the numerical methodology by ensuring direct comparability between numerical predictions and experimentally observed erosion patterns. Fig. 1 presents the erosion patterns observed at the end of the experiment for the selected cases. The top row displays the entire impeller, while the bottom row focuses on a single blade, highlighting the extent and distribution of cavitation-induced erosion.

The observations about experiments are summarized as follows:

- In Case#1, erosion was minimal, with only slight paint removal in the marked region.
- In Case#2, erosion was concentrated at the blade root. Weak pitting also developed in the mid-section of the blades.
- Case#3 had the most severe cavitation erosion. Extensive sheet erosion caused significant paint removal in the sheet region, while root erosion was similar to that in Case#2.
- There are signs of damage at the blade tips (marked in yellow), where painting is challenging. Hence, it is difficult to determine whether these marks result from cavitation erosion.
- Singular marks colored in blue are also present, which are not attributed to cavitation erosion but rather imperfections in the test procedure.

3. Methodology

3.1. Numerical setup

Numerical simulations are conducted using Simcenter STAR-CCM+ to solve the Reynolds-Averaged Navier-Stokes (RANS) equations for incompressible and cavitating turbulent flow. Since the governing equations for these models are extensively documented in the literature (Siemens Digital Industries Software, 2024), they are not explicitly provided here. This study uses the Shear Stress Transport (SST) k-ω turbulence model (Menter, 1993), the Volume of Fluid (VOF) method (Siemens Digital Industries Software, 2024) for multiphase modelling, and the Schnerr-Sauer model (Schnerr and Sauer, 2001) for cavitation prediction.

The VOF method is employed to solve for the volume fraction of three phases: liquid water, vapor, and non-condensable air. Air is included in the simulation to replicate experimental conditions, as discussed in later sections. In this study, the volume fraction equation is discretized using a first-order High-Resolution Interface Capturing (HRIC) scheme. While this scheme can introduce some numerical diffusivity in the downstream air-water interface, this region is not the primary focus of the analysis. The densities of liquid water (ρ_l), vapor (ρ_v), and air (ρ_a) are 998.2, 0.59, and 1.18 [kg/m^3], respectively. Their dynamic viscosity values are 1.1386×10^{-3}, 1.26×10^{-5}, and 1.85×10^{-5} [Pa·s], respectively.

The Schnerr-Sauer cavitation model describes liquid-vapor phase transitions, modeling mass transfer by considering numerous small bubbles undergoing pressure-dependent phase changes (Schnerr and Sauer, 2001). The mass transfer rate between the liquid and vapor phases is defined as:

$$\dot{m} = \begin{cases} C_v \rho_l \frac{3\alpha_v(1-\alpha_v)}{R_b}\sqrt{\frac{2}{3}\frac{|p-p_v|}{\rho_l}}, & p < p_v \quad \text{(vaporization)} \\ C_c \rho_l \frac{3\alpha_v(1-\alpha_v)}{R_b}\sqrt{\frac{2}{3}\frac{|p-p_v|}{\rho_l}}, & p > p_v \quad \text{(condensation)} \end{cases} \tag{2}$$

where $\dot{m}$ is the mass transfer rate in [kg/s], and the vaporization and condensation coefficients, C_v and C_c, are both set to 1.0. The vapor volume fraction is represented by α_v, and the bubble radius, R_b, is assumed to be 1.0×10^{-6} m. The local pressure is denoted as p, and the saturation pressure is set to $p_v = 2065$ Pa. To improve stability and computational efficiency, the model neglects surface tension and slip velocity between the phases.

In RANS modelling of cavitating flows, turbulent viscosity is often overestimated near cavity closure. This leads to poor predictions of critical flow phenomena such as re-entrant jet formation and cavity shedding (R. Fortes-Patella and Reboud, 2002; Bensow, 2011). To address this issue, Reboud's correction (Reboud et al., 1998) is applied. This approach reduces eddy viscosity in regions with high vapor content. The ad hoc correction scales the turbulent viscosity, μ_t, using a density-based scaling factor $f(\rho)$:

$$\mu_t^* = f(\rho) \cdot \mu_t \tag{3}$$

Here, μ_t^* is the corrected turbulent viscosity, and $f(\rho)$ is the scaling function defined as,

$$f(\rho) = \frac{1}{\rho}\left[\rho_v + \frac{(\rho - \rho_v)^n}{(\rho_l - \rho_v)^{n-1}}(\rho_l - \rho_v)\right] \tag{4}$$

The mixture density ρ represents the local density in the computational cell, while the exponent n is an empirical coefficient and is set to 10.

The simulations use an implicit unsteady framework with a second-order temporal discretization to capture transient cavitation dynamics accurately (Siemens Digital Industries Software, 2024). The governing equations are discretized using the finite volume method, and the solution is advanced in time using a pressure-based segregated solver. The Semi-Implicit Method for Pressure-Linked Equations-Consistent (SIMPLEC) algorithm is employed for pressure-velocity coupling.

For spatial discretization, the momentum equations are solved using a second-order upwind scheme, ensuring accurate convection term resolution. The volume fraction equation is discretized using a first-order scheme as recommended by Schnerr and Sauer (2001). The turbulence model transport equations for the SST k-ω model are solved using a second-order scheme for convection terms.

The time step is set to 3.47×10^{-5} s, which corresponds to a rotational resolution of 0.25° per time step, resulting in 1440 time steps per full revolution of the rotor. This motion is modeled using a sliding mesh approach to provide a rotation rate of 20 rps.

Erosion assessments and statistical analyses begin after the initial transients have settled and continue for a duration of 10 revolutions.

3.2. Cavitation erosion assessment

This study uses a cavitation erosion risk assessment tool developed in earlier work (Özgünoğlu et al., 2025), originally validated for cavitation erosion in high-pressure fuel injectors. The model evaluates erosion risk by using the squared material derivative of pressure, $(DP/Dt)^2$, as a key indicator. This metric captures rapid and localized pressure transients arising during bubble collapse (Brennen, 2013) – whether caused by shock-like implosions or micro-jets impacting surfaces. While incompressible formulations do not resolve true shock waves, they capture strong pressure pulses that contribute to erosion. Squaring (DP/Dt) enhances sensitivity to high-pressure fluctuations, making it effective for identifying erosion-prone regions.

The method identifies erosion regions by applying three conditions to all computational cells (Fig. 2). First, vapor volume fraction must drop to zero over three consecutive time steps ($\alpha_{t_{n-2}} > 0, \alpha_{t_{n-1}} = 0, \alpha_{t_n} = 0$), ensuring detection of local collapses rather than convected vapor. Second, $(DP/Dt)^2$ must show increasing intensity over time. Third, a negative mass transfer rate ($R < 0$) confirms vapor condensation. This approach refines the work of Mihatsch et al. (2013) and Mouvanal et al. (2018) by incorporating $(DP/Dt)^2$ for better erosion prediction.

Once all conditions are met, the algorithm records the peak $(DP/Dt)^2$ value for each cell throughout the simulation, storing the highest recorded value. In STAR-CCM+, the model is implemented using field functions which allow seamless integration. For further details and validation of the methodology, readers are referred to the previous work (Özgünoğlu et al., 2025).

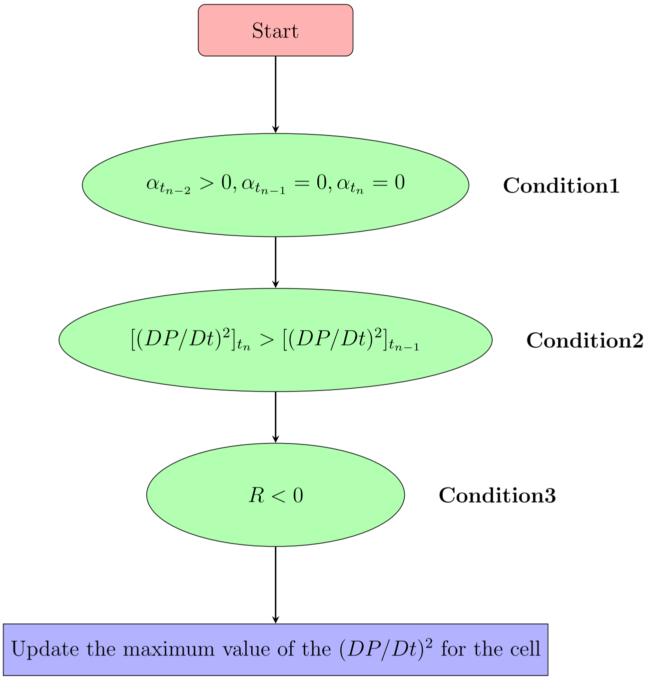

Fig. 2. Cavitation erosion algorithm.

Table 2
Boundary conditions.

Studied case	Inlet Velocity (m/s)	Outlet Pressure (Pa)
Case#1	3.725	18,600
Case#2	5.529	11,800
Case#3	6.681	17,000

3.3. Geometry and boundary conditions

Fig. 3 illustrates the main topology of the computational domain. The flow enters through a rectangular inlet channel and splits into two primary streams. One stream flows into the rotor region through a flush-type intake duct, while the remaining flow continues toward the tunnel outlet.

The inlet is defined as a velocity inlet, while the pump and tunnel outlets are set as pressure outlets. To ensure consistency with the experimental setup, the inlet velocity values in the simulations match the tunnel velocities measured approximately 1400 mm upstream of the inlet lip. Table 2 presents the velocity and pressure values used in the simulations, corresponding to the experimental operating conditions in Table 1.

Despite relatively shallow depth of the tunnel outlet's, hydrostatic effects are incorporated by implementing a hydrostatic boundary condition at the outlet. The reference location for hydrostatic pressure is defined at the rotor axis. This boundary condition had a noticeable impact on the results, as using the hydrostatic pressure profile instead of a constant tunnel pressure value led to a decrease in total vapor volume within the rotor region.

The back pressure on the pump outlet influences the cavitation dynamics and cavitation erosion behavior by affecting the pressure distribution and vapor collapse characteristics. In this study, the air is included primarily to provide realistic tunnel pressure (which was measured with air volume) conditions in the experiment. A no-slip boundary condition is applied to the pump casing, hub, stator, duct, and upper tunnel walls. The tunnel's side and bottom surfaces are set as slip boundaries. Rotating and stationary regions interact through predefined interfaces.

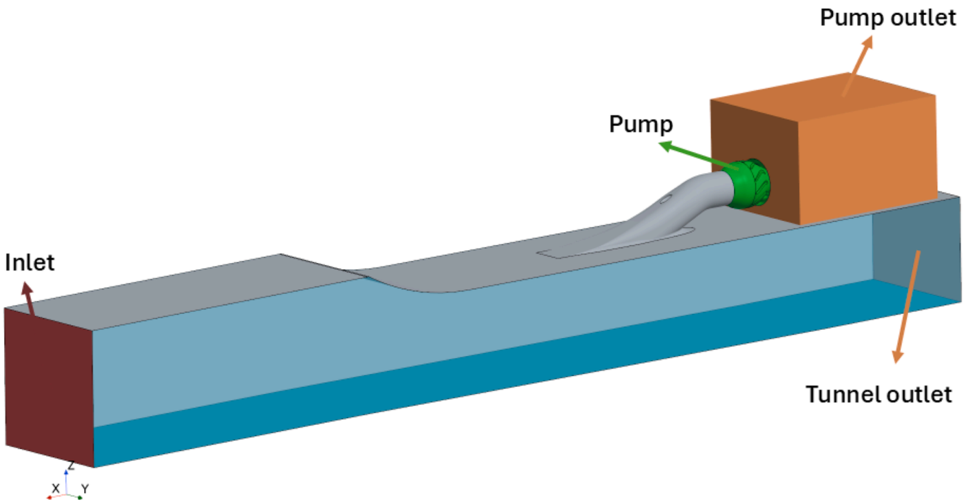

Fig. 3. Geometry and boundary conditions.

Fig. 4. Representation of the root and sheet region on selected blade.

Besides the aforementioned cavitation erosion assessment using the maximum $(DP/Dt)^2$ values on the surfaces, the pitting behavior on the rotor blades is additionally investigated. In this analysis, one blade is selected and divided into two distinct regions: the sheet region and the root region, as transparently illustrated in Fig. 4. The sheet region, highlighted in green, represents the larger portion of the blade, while the root region, shown in red, corresponds to the section near the hub. The force acting on these surfaces was integrated separately for each case to assess the localized effects of flow and cavitation dynamics.

To facilitate a meaningful comparison between different regions, the total force acting on each region was normalized by the corresponding surface area. This normalization ensures that the force values are independent of the size of each region, allowing for a "pressure-like" interpretation. The normalized force per unit area, denoted as $\bar{F}$, is computed as:

$$\bar{F} = \frac{F_{\text{region}}}{A_{\text{region}}} \tag{5}$$

where F_{region} represents the integrated force acting on either the "sheet" or "root" region, and A_{region} denotes the corresponding surface area.

3.4. Computational domain

To assess the effect of grid resolution on numerical simulations, three computational grids were generated and tested with Case#3 condition. These grids, labeled as Baseline, Coarse, and Refined, differ in spatial resolution and total cell count. Table 3 summarizes the number of cells in different regions of the computational domain.

In the coarse grid, the base size was set to 1/50 of the rotor diameter (0.27 m), resulting in a 5.4 mm. The baseline grid further halved the base cell size, achieving a 2.7 mm grid resolution. The Refined grid was obtained by further refining only the rotating region while keeping the inlet and outlet channels identical to the Baseline configuration.

Table 3
Number of cells for different regions of the computational domain for different grid configurations.

Region	Coarse	Baseline	Refined
Inlet channel	4.0×10^6	15.7×10^6	15.7×10^6
Outlet channel	1.3×10^6	4.1×10^6	4.1×10^6
Rotating region	2.7×10^6	7.0×10^6	19.4×10^6
Total Cells	8.0×10^6	26.8×10^6	39.2×10^6

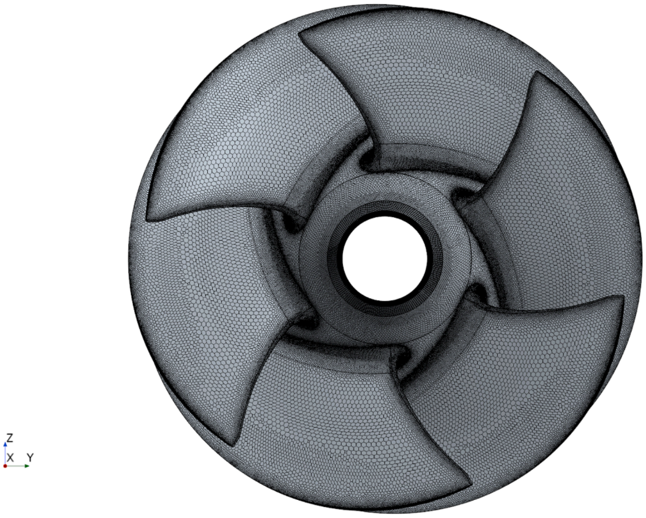

Fig. 5. Surface mesh representation of the impeller.

Fig. 5 presents impeller surface mesh of the Baseline grid. The inlet channel primarily utilizes hexahedral cells, generated using a trimmed cell mesher. Meanwhile, the rotating impeller region and outlet channel are meshed using polyhedral cells, allowing for better adaptability to complex geometries and improved numerical stability.

Table 4 presents the total vapor volume and vapor flow rate for different grid resolutions. Despite varying grid refinement levels, the total vapor volume and volume flow rates remain nearly identical, indicating consistent numerical predictions across different mesh configurations. The flow rate predictions obtained from the numerical simulations are also compared with the experimental flow rate of 0.15648 m^3/s. The results showed that each grid shows around 1–2 % deviation from the

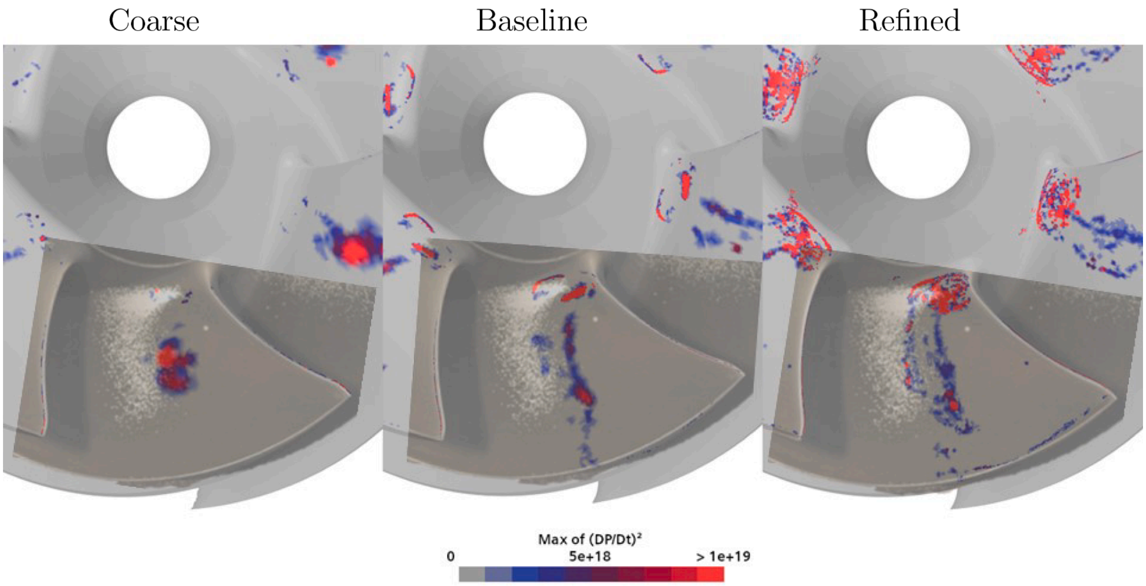

Fig. 6. Comparison of maximum $(DP/Dt)^2$ values for cavitation erosion prediction using different grid resolutions. The experimental images are overlaid transparently for direct visual correlation.

Table 4
Comparison of total vapor volume and volume flow rate for each grid configurations.

Grid	Total vapor volume (mm^3)	Volume flow rate (m^3/s)
Coarse	4456	0.1546
Baseline	4375	0.1547
Refined	4252	0.1545

experimental flow rate. Despite the finer grid resolution, the improvement in flow rate prediction remained limited, indicating that all grids capture the systematic flow properties with sufficient accuracy.

To further evaluate the effect of grid resolution on cavitation erosion predictions, a comparative analysis was conducted across all grid configurations. Fig. 6 presents the maximum values of the $(DP/Dt)^2$ for the coarse, baseline, and refined grids. The refined grid captures wider erosion patterns over the sheet region. In contrast, the coarse grid failed to capture the root erosion observed in the experiment (see Fig. 1, Case#3). Thus, the refined grid aligns more closely with the experimental observations.

While further grid refinement is theoretically possible, as demonstrated in LES studies by Arabnejad et al. (2022, 2020), achieving LES-level accuracy requires significantly higher resolutions. These studies emphasize the need for higher grid resolutions to resolve the turbulent structures accurately. In particular, they highlight that at least 40 cells inside the tip gap are necessary to successfully capture the Tip Leakage Vortex (TLV) phenomena. However, this study aims to provide a reliable erosion assessment tool while ensuring computational efficiency. The use of RANS-based modeling makes it a viable approach for industrial applications. It is clear from the Fig. 6 that although the refined grid captures more detailed erosion zones, the baseline grid provides sufficient accuracy with an acceptable resolution. Therefore, considering the overall computational cost of all simulations, all subsequent simulations will be conducted using the baseline grid.

4. Results and discussion

Fig. 7 presents the total vapor volume percentage over one full revolution for all cases. The percentage is calculated by normalizing the total vapor volume within the rotor zone with respect to the total volume of the rotor zone. The plot shows that Case#1 exhibits the highest vapor content, followed by Case#2, while Case#3 has the lowest vapor volume. These trends suggest that cavitation behavior is strongly affected by inlet velocity and pressure conditions. The periodic peaks in vapor volume suggest a possible correlation with each blade passing through a critical region. This behavior is more pronounced in Case#2 and Case#3, where the inlet velocity is higher. It will be shown that the six periodic peaks per revolution indicate that each blade is passing through the region in the upper part of the rotor, where the shaft wake disrupts the local flow and influences cavitation formation.

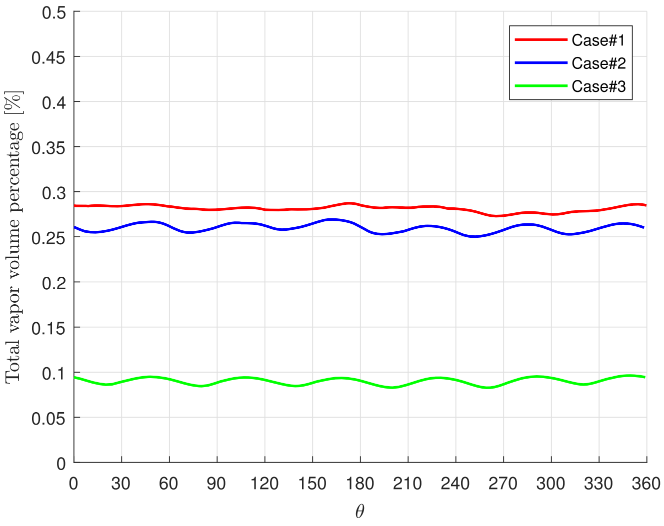

Fig. 7. Total vapor volume percentage over one full revolution for all cases.

Fig. 8 presents the axial velocity field (left) and pressure (right) on the cut-plane between the duct-rotor interface and the rotor blades. Both fields reveal flow asymmetry, which becomes more pronounced as the inlet velocity increases. The asymmetry is more distinct in Case#2 and Case#3 compared to Case#1, where the inlet velocity is lower. Higher inlet velocities in these cases increase the wake effects and alter the flow field, leading to variations in the incoming velocity distribution. This affects how each rotor blade interacts with the flow and ultimately influences the angle of attack as the blades rotate through

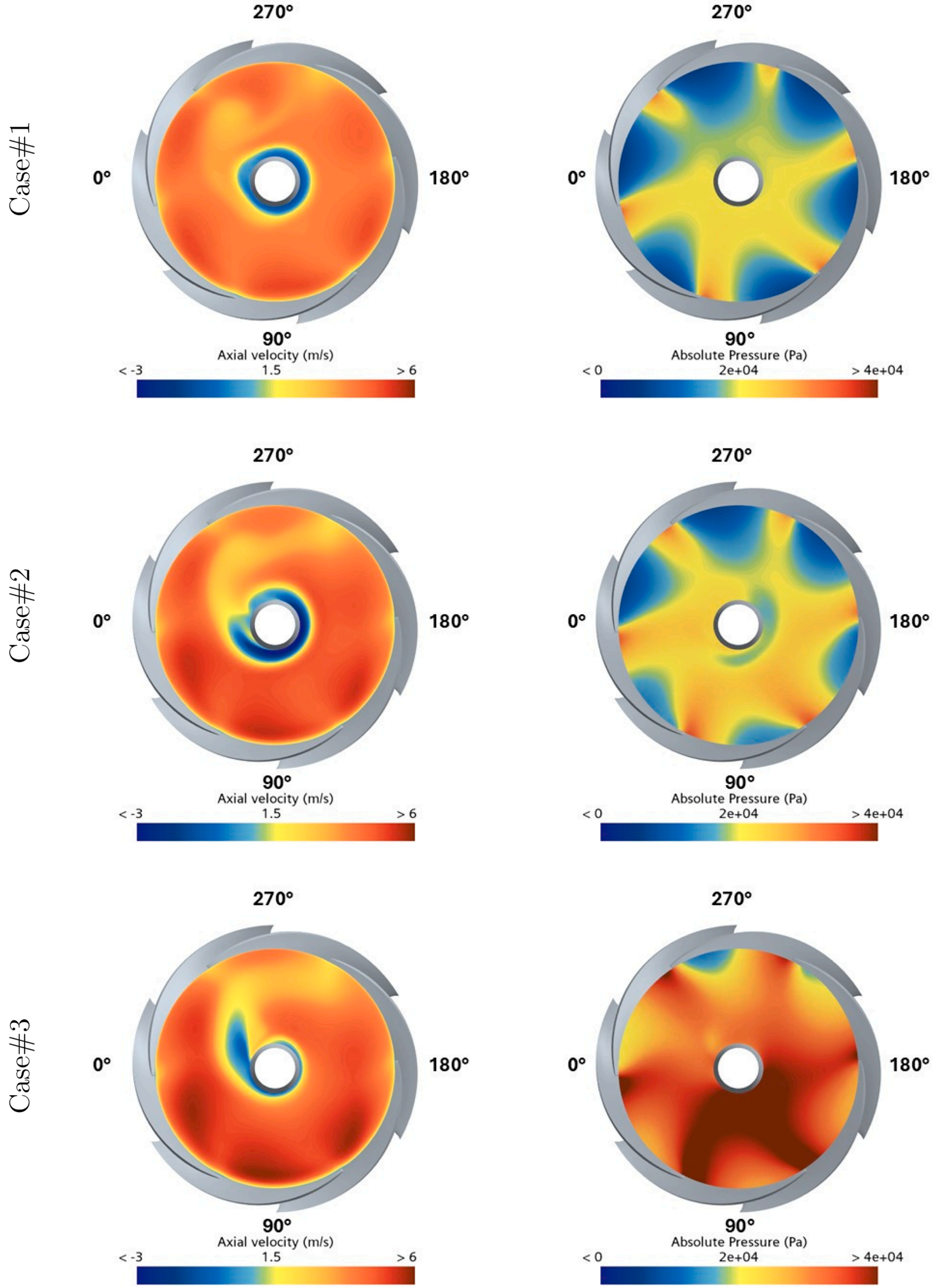

Fig. 8. Axial velocity (left) and pressure (right) on the cut-plane between the duct - rotor interface and the rotor blades.

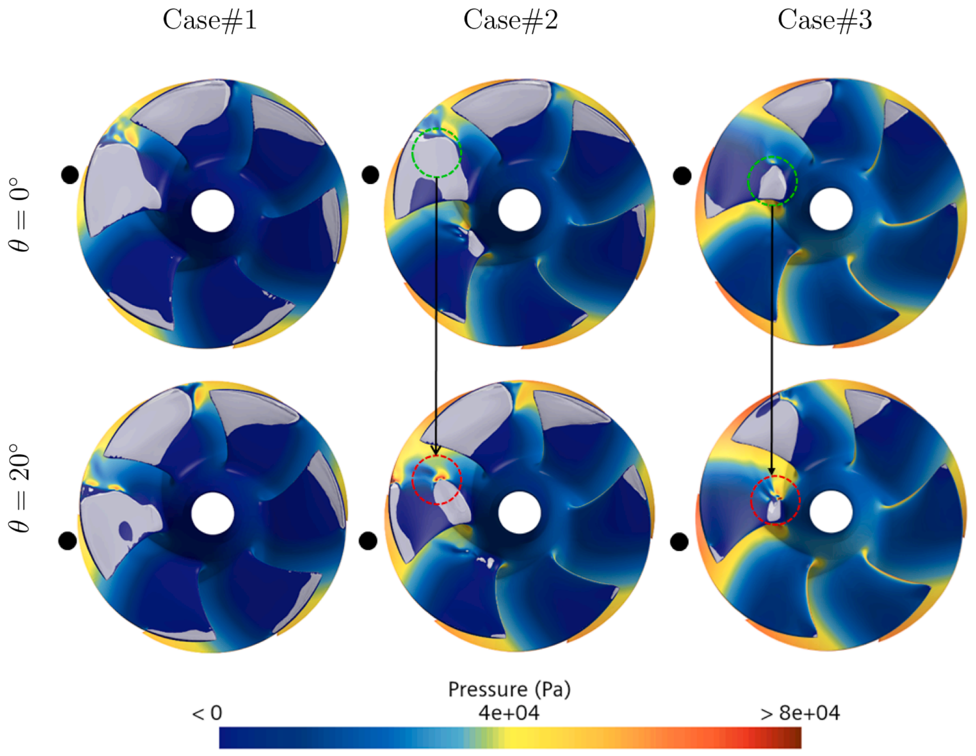

Fig. 9. Instantaneous pressure distribution and vapor isosurfaces (α = 0.5) – I.

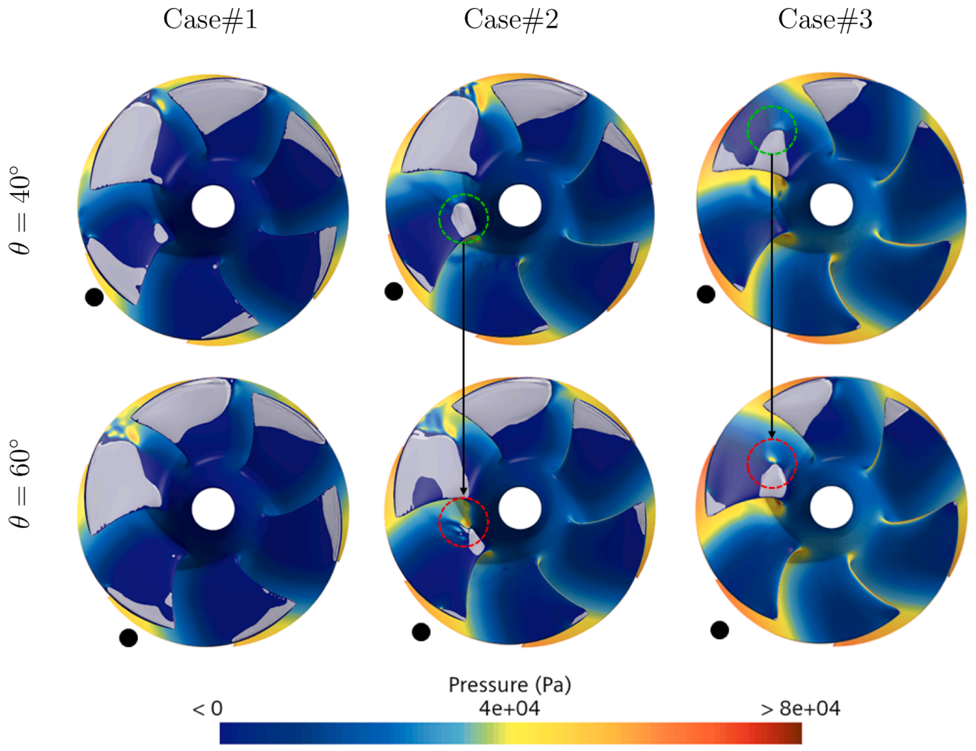

Fig. 10. Instantaneous pressure distribution and vapor isosurfaces (α = 0.5) – II.

different positions (Arabnejad et al., 2022). The most significant impact occurs at 270°, where the wake of the shaft is most dominant. An attempt was made to visualize vortex structures, similar to the approach of Arabnejad et al. (2022). However, due to inability of RANS to resolve unsteady vortical structures, these features could not be captured in detail.

On the right side, the absolute pressure distribution confirms that the lower half of the rotor (0° – 180°) consistently acts as a pressure recovery region. In Case#3, the entire rotor region shows elevated pressures compared to Case#1 and Case#2, reflecting stronger pressure recovery and wake interaction effects. Although the upper region (180° – 360°) still exhibits relatively lower-pressure zones that support cavitation

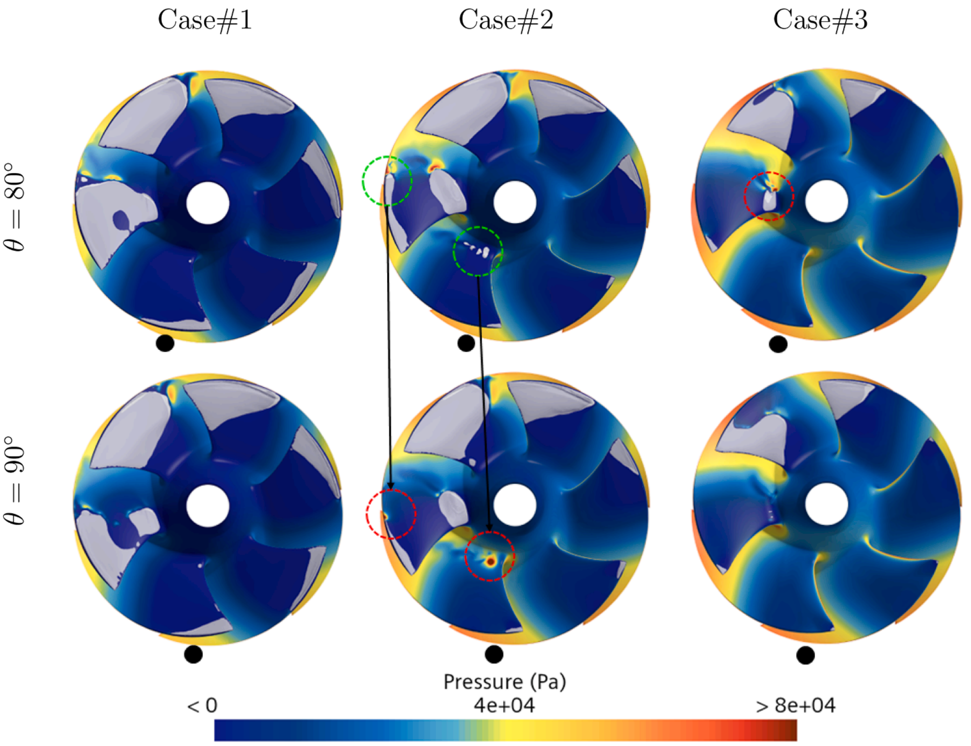

Fig. 11. Instantaneous pressure distribution and vapor isosurfaces ($\alpha = 0.5$) – III.

development, the contrast between high and low pressure is less distinct in Case#3 due to the globally elevated pressure field.

Figs. 9–11 show the instantaneous pressure distribution and vapor isosurfaces at different blade positions (0°, 20°, 40°, 60°, 80°, and 90°). Each row represents a time snapshot over a quarter revolution. The marked regions highlight key dynamics: Green circles indicate vapor structures, while red circles identify collapse instances, capturing the moment of vapor implosion. The black arrows illustrate the sequential relationship between vapor formation and its subsequent collapse. The supplementary materials provide the full revolution as an animation.

The effect of different operating conditions is evident across the cases. The size of the vapor structures varies and is consistent with Fig. 7. For all cases, starting from 270°, a sheet cavity forms along the leading edge of the blades. As the blade continues its rotation, the sheet cavity grows, reaching its maximum size around 0°. Beyond this point, the sheet cavity shrinks as the local pressure increases, following the pressure recovery trend observed in Fig. 8. At 90°, the sheet cavity is almost entirely dissipated, except for a remaining root cavity, which eventually collapses as the blade moves forward. This cyclic behavior of cavity growth and collapse establishes a clear correlation between blade position and cavitation intensity.

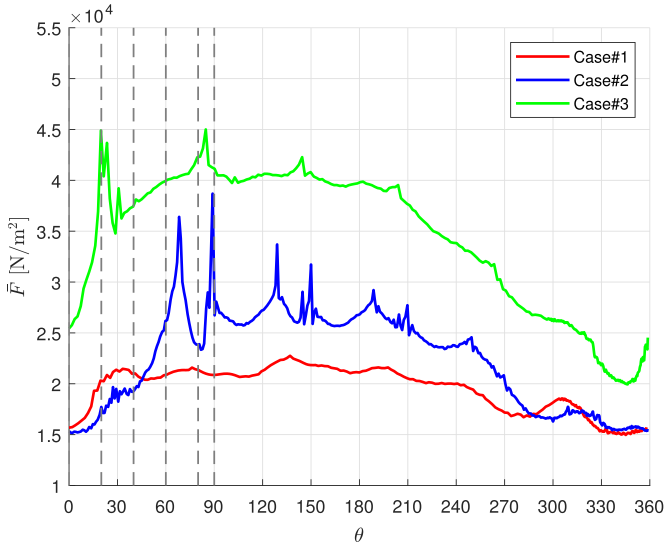

Fig. 12. Temporal evolution of the normalized root force ($\bar{F}$) over one full revolution for all cases. The dashed lines correspond to the time instants selected in Figs. 9–11.

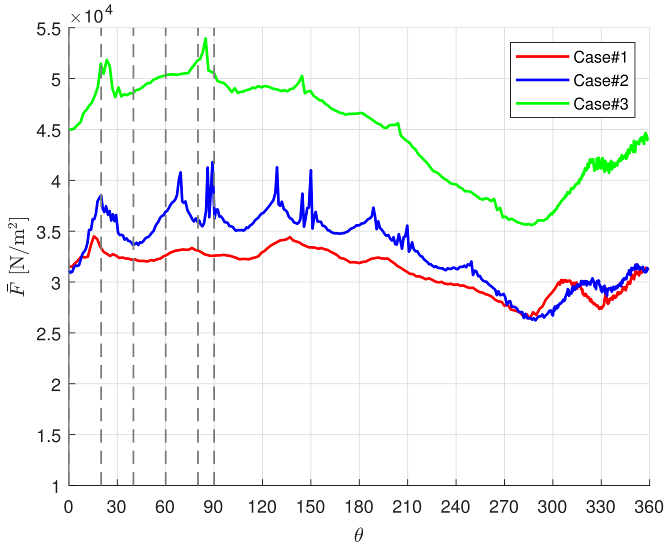

Fig. 13. Temporal evolution of the normalized sheet force ($\bar{F}$) over one full revolution for all cases. The dashed lines correspond to the time instants selected in Figs. 9–11.

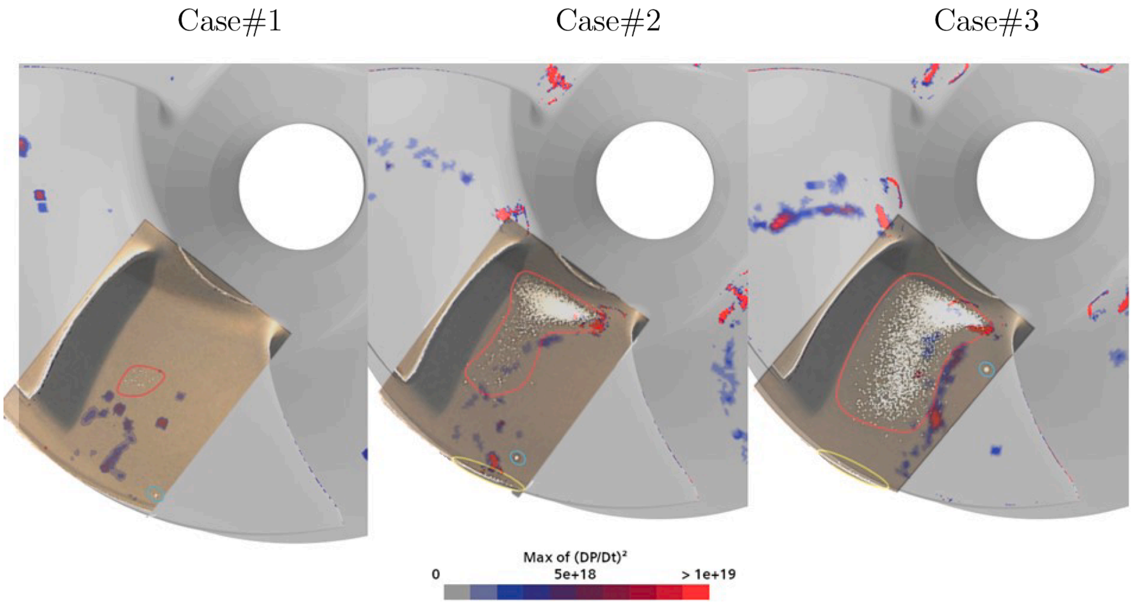

Fig. 14. Comparison of the numerical erosion predictions with experimental erosion patterns (in Fig. 1) for all cases. The experimental images are overlaid transparently for direct visual correlation.

While these findings align with previous research on this geometry under different operating conditions, notable differences arise when compared with the LES-based study by Arabnejad et al. (2022). LES captures more intermittent and isolated cavitation shedding behaviors, whereas RANS limits shedding to a more averaged, mean behavior, despite the reduction of turbulent viscosity. The vapor structures observed in Figs. 9–11 exhibit limited variation over time compared to LES predictions, indicating that cavitation shedding in RANS simulations follows a more periodic and deterministic pattern. Previous LES studies suggest that cavitation clouds detach more frequently, contributing to stronger pressure pulses and a more dynamic collapse process (Arabnejad et al., 2022; Yang et al., 2025). In contrast, the current RANS-based approach primarily predicts large-scale, quasi-steady cavities that do not fully capture the finer-scale interactions governing cavitation dynamics. This highlights a key limitation of RANS in resolving the transient evolution of vapor structures, which directly influences the spatial resolution of the erosion assessment.

Figs. 12 and 13 show the time evolution of the normalized forces on the root and sheet regions. The dashed lines correspond to the selected time instants in Figs. 9–11, where the tracked blade is marked with a large black point. These plots provide insight into two important aspects: the local minima, which reveal how the fluid pressure acts on the tracked blade as it moves, and the local maxima, which indicate sudden force spikes associated with cavitation collapse events. The local minima in the force plots indicate the gradual variation in pressure along the blade path. As the blade moves from 0° to 90°, there is a noticeable increase in normalized force (both root and sheet), aligning with the previously discussed pressure recovery in this region. However, beyond 90°, as the blade continues toward 270°, the pressure decreases, suggesting that the cavitation generation is more pronounced. The local maxima, represented by sharp spikes in the force plots, provide critical information about cavitation collapse events. These peaks are particularly pronounced in Case#2 and Case#3, where high-pressure fluctuations suggest intense vapor collapse. The largest force spikes occur in the first quarter of the revolution ($0^\circ - 90^\circ$). The occurrence of these force peaks aligns well with the collapse instances marked in Figs. 9–11.

Finally, Fig. 14 compares the numerically predicted erosion risk zones with experimental paint test results. Case#3 exhibits the most severe erosion, particularly near the root and sheet regions, which aligns with strong cavitation collapse events. Case#2 shows notable erosion, mainly near the impeller tip, whereas Case#1 shows minimal erosion, consistent with its stable normalized force trends.

In numerical predictions, the effects of operating conditions are reflected, and distinct numerical erosion patterns are observed for each case. This confirms that the proposed methodology performs well in capturing the influence of flow parameters on cavitation erosion risk. However, the overall size of the predicted erosion zones is under-predicted, especially for Case#2 and Case#3. While experimental results indicate larger erosion regions, numerical predictions confine damage zones to more localized areas. This discrepancy is directly related to the cavitation shedding behavior discussed earlier in Figs. 9–11.Arabnejad et al. (2022) demonstrated that cavitation clouds shed more intermittently and dynamically, leading to stronger pressure pulses and more widespread erosion regions. However, in RANS-based simulations, even with reductions in turbulent viscosity, shedding behavior is restricted to a mean representation, limiting the extent of cavitation-induced erosion.

5. Conclusion

This study presents a numerical cavitation erosion assessment for a water-jet pump using a Reynolds-Averaged Navier-Stokes (RANS) approach, the Schnerr-Sauer cavitation model, and an erosion risk assessment tool validated in prior research (Özgünoğlu et al., 2025). The numerical results were compared against experimental soft paint erosion tests conducted in a free-surface cavitation tunnel to evaluate predictive performance.

The findings confirm that the numerical approach effectively captures the influence of operating conditions on cavitation behavior. Variations in inlet velocity and pressure conditions strongly affect cavitation structures, with Case#1 exhibiting the highest vapor content and Case#3 the lowest. The vapor volume distribution aligns with blade passage through critical flow regions, particularly where the shaft wake disrupts local flow and promotes cavitation formation. The axial velocity and pressure fields further reveal increasing asymmetry at higher inlet velocities, altering blade interactions and affecting cavitation intensity.

The erosion risk metric based on $(DP/Dt)^2$ successfully identifies characteristic cavitation erosion zones, particularly in the sheet and root regions. However, while the numerical model correctly predicts the locations of high-risk areas, it consistently underestimates the overall extent and size of erosion zones, particularly in Case#2 and Case#3. This discrepancy is attributed to the deterministic nature of cavitation shedding in RANS-based simulations, which fail to reproduce the intermittent shedding observed experimentally. The lack of re-entrant jet interactions and the inability to resolve small-scale cavity collapses further contribute to the under-prediction of erosion extent.

A detailed normalized force analysis highlights the presence of sharp force peaks, particularly in Case#2 and Case#3, where strong pressure fluctuations due to cavity collapses drive erosion formation. The largest force spikes occur between 0° and 90° rotation, aligning with vapor collapse instances. While this aligns with expected erosion-prone zones, the magnitude of predicted forces suggests a more localized impact compared to the broader erosion regions observed experimentally.

The primary limitation of the present approach lies in the use of RANS-based turbulence modeling. While RANS efficiently captures mean flow characteristics and global cavitation trends, it struggles to resolve transient cavitation structures and secondary flow effects, which play a crucial role in cavitation erosion mechanisms. Compared to the previous LES study (Arabnejad et al., 2022), RANS models fail to account for the dynamic evolution of cavitation clouds, leading to a more periodic and deterministic representation of cavitation shedding. The inability to capture high-frequency pressure pulses limits the accuracy of erosion predictions, particularly in cases with strong unsteady flow interactions.

Despite these limitations, the proposed RANS-based framework provides a computationally efficient early-stage assessment tool for evaluating cavitation erosion risks in industrial applications. While it cannot fully resolve unsteady cavitation dynamics, it enables rapid identification of erosion-prone regions, allowing engineers to perform preliminary design assessments before resorting to high-fidelity simulations.

Despite some discrepancies in erosion extent and location, the RANS-based framework effectively captures the influence of operating conditions on cavitation behavior. This demonstrates its capability as a practical tool for early-stage assessments, potentially extending its applicability to geometry optimization and pump design.

Future research should focus on refining turbulence modeling strategies, incorporating hybrid RANS-LES approaches, and integrating more advanced erosion models to improve predictive accuracy. Additionally, extending the methodology to a wider range of pump configurations and operating regimes would enhance its applicability in real-world engineering problems.

CRediT authorship contribution statement

Mehmet Özgünoğlu: Conceptualization, Methodology, Software, Validation, Investigation, Writing – original draft, Visualization; **Martin Persson:** Writing – review & editing, Software, Methodology, Conceptualization; **Ammar Saber:** Writing – review & editing, Supervision; **Rickard E. Bensow:** Supervision, Writing – review & editing, Funding acquisition.

Declaration of competing interest

The authors declare that they have no known competing financial interests or personal relationships that could have appeared to influence the work reported in this paper.

Acknowledgment

The computations were enabled by the resources provided by Chalmers e-Commons at Chalmers University of Technology and the National Academic Infrastructure for Supercomputing in Sweden (NAISS), partially funded by the Swedish Research Council through grant agreement no. 2022–06725.

References

Aktas, B., Usta, O., Atlar, M., 2020. Systematic investigation of coating application methods and soft paint types to detect cavitation erosion on marine propellers. Appl. Ocean Res. 94, 101868. https://doi.org/10.1016/j.apor.2019.101868

Alves Pereira, F., Boucheron, R., Boucetta, D., Fetherstonhaugh, C., Krol, P., Pang, Y., Park, C., Sato, K., Straka, W.A., Viitanen, V., 2024. Cavitation Induced Erosion on Propellers and Rudders, Model Scale Experiments and Numerical Guidance. Technical Report 7.5-02-03-03.5. International Towing Tank Conference ITTC. Switzerland. ITTC Recommended Procedures and Guidelines, Revision 03.

Arabnejad, M., Eslamdoost, A., Svennberg, U., Bensow, R., 2020. Scale resolving simulations of the non-cavitating and cavitating flows in an axial water jet pump. In: 33nd Symposium on Naval Hydrodynamics, pp. 19–23.

Arabnejad, M.H., Svennberg, U., Bensow, R.E., 2021. Numerical assessment of cavitation erosion risk using incompressible simulation of cavitating flows. Wear 464–465, 203529. https://doi.org/10.1016/j.wear.2020.203529

Arabnejad, M.H., Svennberg, U., Bensow, R.E., 2022. Numerical assessment of cavitation erosion risk in a commercial water-jet pump. J. Fluids Eng. 144 (5), 051201. https://doi.org/10.1115/1.4052634

Bark, G., Bensow, R.E., 2013. Hydrodynamic mechanisms controlling cavitation erosion. Int. Shipbuild. Progress 60, 345–374. https://doi.org/10.3233/ISP-130097

Bark, G., Berchiche, N., Grekula, M., 2004. Application of principles for observation and analysis of eroding cavitation-the EROCAV observation handbook. EROCAV Report, Dept. of Naval Architecture, Chalmers University of Technology, Göteborg, Sweden.

Bensow, R.E., 2011. Simulation of the unsteady cavitation on the Delft twist11 foil using RANS, DES and LES. In: Second International Symposium on Marine Propulsors. Hamburg, Germany.

Bensow, R.E., 2021. Chapter 4 - numerical prediction of cavitation and related nuisances in marine propulsion systems. In: Koukouvinis, P., Gavaises, M. (Eds.), Cavitation and Bubble Dynamics. Academic Press, pp. 111–132. https://doi.org/10.1016/B978-0-12-823388-7.00006-0

Brennen, C.E., 2013. Cavitation and Bubble Dynamics. Cambridge University Press, Cambridge. chapter 3. pp. 59–88.

Budich, B., Schmidt, S., Adams, N., 2015. Numerical simulation of cavitating ship propeller flow and assessment of erosion aggressiveness. In: Proceedings of MARINE 2015 - Computational Methods in Marine Engineering VI. CIMNE, pp. 709–721.

Cao, P., Wang, Y., Kang, C., Li, G., Zhang, X., 2017. Investigation of the role of non-uniform suction flow in the performance of water-jet pump. Ocean Eng. 140, 258–269. https://doi.org/10.1016/j.oceaneng.2017.05.034

Coutier-Delgosha, O., Fortes-Patella, R., Reboud, J.L., 2002. Simulation of unsteady cavitation with a two-equation turbulence model including compressibility effects. J. Turbulence 3, N58. https://doi.org/10.1088/1468-5248/3/1/058

Franc, J.-P., Michel, J.-M., 2004. Fundamentals of Cavitation. Vol. 76 of *Fluid Mechanics and Its Applications*. Springer Dordrecht. https://doi.org/10.1007/1-4020-2233-6

Huang, R., Wang, Y., Du, T., Luo, X., Zhang, W., Dai, Y., 2021. Mechanism analyses of the unsteady vortical cavitation behaviors for a waterjet pump in a non-uniform inflow. Ocean Eng. 233, 108798. https://doi.org/10.1016/j.oceaneng.2021.108798

Ji, B., Wang, Z.-y., Cheng, H.-y., Bensow, R.E., 2024. Cavitation research with computational fluid dynamics: from euler-euler to euler-lagrange approach. J. Hydrodyn. 36, 1–23. https://doi.org/10.1007/s42241-024-0001-2

Kaixuan, Z., Yun, L., Qingjiang, X., Changjian, X., Jianping, C., Dezhong, W., 2024. Study on the experiment and numerical simulation of cavitation flow mechanisms at different flow rates in water-jet propulsion pumps. J. Phys. 2707 (1), 012050. https://doi.org/10.1088/1742-6596/2707/1/012050

Kleinsorge, L., Peters, A., Schreiner, F., Greitsch, L., Moctar, O.e., Skoda, R., 2022. Numerical prediction of cavitation erosion on ship propulsors. In: Proceedings of the 7th International Symposium on Marine Propulsors (smp'22), pp. 436–441.

Koksal, C.S., Usta, O., Aktas, B., Atlar, M., Korkut, E., 2021. Numerical prediction of cavitation erosion to investigate the effect of wake on marine propellers. Ocean Eng. 239, 109820. https://doi.org/10.1016/j.oceaneng.2021.109820

Li, Z.-r., Pourquie, M., van Terwisga, T., 2014. Assessment of cavitation erosion with a URANS method. J. Fluids Eng. 136 (4), 041101. https://doi.org/10.1115/1.4026195

Melissaris, T., Bulten, N., van Terwisga, T.J.C., 2019. On the applicability of cavitation erosion risk models with a URANS solver. J. Fluids Eng. 141 (10), 101104. https://doi.org/10.1115/1.4043169

Melissaris, T., Schenke, S., Bulten, N., van Terwisga, T.J.C., 2022. Cavitation erosion risk assessment on a full-scale steerable thruster. Ocean Eng. 251, 111019. https://doi.org/10.1016/j.oceaneng.2022.111019

Melissaris, T., Schenke, S., Bulten, N., van Terwisga, T.J.C., 2020. On the accuracy of predicting cavitation impact loads on marine propellers. Wear 456–457, 203393. https://doi.org/10.1016/j.wear.2020.203393

Menter, F.R., 1993. Zonal two equation $k-\omega$ Turbulence Models for aerodynamic flows. In: 24th Fluid Dynamics Conference. Orlando, FL. https://doi.org/10.2514/6.1993-2906

Mihatsch, M.S., Schmidt, S.J., Thalhamer, M., Adams, N.A., 2013. Numerical Prediction of Erosive Collapse Events in Unsteady Compressible Cavitating Flows. Springer Netherlands, Dordrecht. chapter 39. pp. 499–510. https://doi.org/10.1007/978-94-007-6143-8_39

Mouvanal, S., Chatterjee, D., Bakshi, S., Burkhardt, A., Mohr, V., 2018. Numerical prediction of potential cavitation erosion in fuel injectors. Int. J. Multiphase Flow 104, 113–124. https://doi.org/10.1016/j.ijmultiphaseflow.2018.03.005

Özgünoğlu, M., Mouokue, G., Oevermann, M., Bensow, R.E., 2025. Numerical investigation of cavitation erosion in high-pressure fuel injector in the presence of surface deviations. Fuel 386, 134174. https://doi.org/10.1016/j.fuel.2024.134174

Park, W.-G., Jang, J.H., Chun, H.H., Kim, M.C., 2005. Numerical flow and performance analysis of waterjet propulsion system. Ocean Eng. 32 (14), 1740–1761. https://doi.org/10.1016/j.oceaneng.2005.02.004

Peters, A., Lantermann, U., el Moctar, O., 2018. Numerical prediction of cavitation erosion on a ship propeller in model- and full-scale. Wear 408–409, 1–12. https://doi.org/10.1016/j.wear.2018.04.012

Qiu, N., Zhu, H., Long, Y., Zhong, J., Zhu, R., Wu, S., 2021. Assessment of cavitation erosion in a water-jet pump based on the erosive power method. Scanning 2021. https://doi.org/10.1155/2021/5394782

Reboud, J.-L., Stutz, B., Coutier, O., 1998. Two-phase flow structure of cavitation: experiment and modelling of unsteady effects. In: Proceedings of the 3rd International Symposium on Cavitation (CAV1998). Grenoble, France, pp. 1–8.

Schenke, S., van Terwisga, T.J.C., 2019. An energy conservative method to predict the erosive aggressiveness of collapsing cavitating structures and cavitating flows from numerical simulations. Int. J. Multiphase Flow 111, 200–218. https://doi.org/10.1016/j.ijmultiphaseflow.2018.11.016

Schnerr, G.H., Sauer, J., 2001. Physical and numerical modeling of unsteady cavitation dynamics. In: Fourth International Conference on Multiphase Flow. Vol. 1. ICMF New Orleans New Orleans, LO, USA, pp. 1–12.

Shin, K.W., Andersen, P., 2020. Practical numerical method for erosion risk prediction on ship propellers. Int. Shipbuild. Progress 67, 199–220. https://doi.org/10.3233/ISP-201002

Siemens Digital Industries Software, 2024. Simcenter STAR-CCM+ User Guide v. 19.06–008 (Siemens 2024).

Usta, O., Aktas, B., Maasch, M., Turan, O., Atlar, M., Korkut, E., 2017. A study on the numerical prediction of cavitation erosion for propellers. Proceedings of the Fifth International Symposium on Marine Propulsors. VTT Technical Research Center of Finland.

Usta, O., Korkut, E., 2018. A study for cavitating flow analysis using DES model. Ocean Eng. 160, 397–411. https://doi.org/10.1016/j.oceaneng.2018.04.064

Wang, Z., Cheng, H., Bensow, R.E., Peng, X., Ji, B., 2023. Numerical assessment of cavitation erosion risk on the delft twisted hydrofoil using a hybrid eulerian-lagrangian strategy. Int. J. Mech. Sci. 259, 108618. https://doi.org/10.1016/j.ijmecsci.2023.108618

Wheeler, M., Peters, A., Moctar, B.O.E., Persson, M., Gunderson, A., Frisk, D., Ponkratov, D., 2024. Evaluation of cavitation erosion models on industrial maritime applications using commercial CFD software. In: Proceedings of the International Cavitation Symposium (CAV2024). International Cavitation Symposium.

Xu, H., Chen, Z., Wu, Q., Cai, Y., 2024. A wall-modeled large-eddy simulation of the unsteady flow in a water-jet pump based on the turbulent length scales. Ocean Eng. 313, 119559. https://doi.org/10.1016/j.oceaneng.2024.119559

Xu, Z., Lai, H., 2023. Comparison of cavitation in two axial-flow water jet propulsion pumps. Processes. https://doi.org/10.3390/pr11061678

Yang, Y., Xiong, C., Wang, S., Zhang, A.-M., 2025. Cavitation erosion risk on a hydrofoil using a multi-scale method. Phys. Fluids 37 (2), 027107. https://doi.org/10.1063/5.0242145